ACS APPLIED NANO MATERIALS

www.acsanm.org Article

Nanoporous AlGaN Distributed Bragg Reflectors for Deep Ultraviolet Emission

Maocheng Shan, Chenyu Guo, Yongming Zhao, Qiushuang Chen, Liqiong Deng, Zhihua Zheng, Shizhou Tan, Wei Guo, Jiangnan Dai, Feng Wu,* Xiaohang Li,* and Changqing Chen*

Cite This: *ACS Appl. Nano Mater.* 2022, 5, 10081−10089 Read Online

ABSTRACT: In this paper, we demonstrated wafer-scale AlGaN-based deep ultraviolet (DUV) nanoporous (NP) distributed Bragg reflectors (DBRs) by vertical electrochemical (EC) etching. The stopbands of the NP-DBRs were centered around 280 nm with reflectance close to 90%. A thick AlGaN film and four-period multiple quantum wells (MQWs) were grown on the strain-relaxed NP-DBRs template. The reciprocal space mappings (RSMs) revealed the increased compressive strain in MQWs grown on NP-DBRs, and transverse electric (TE) mode emission was enhanced due to this strain modulation. Thanks to the reflection effect, the photoluminescence (PL) intensity of the MQWs in the NP-DBR region was more than twice that of the region without NP-DBRs. The anisotropic optical polarization measurements and theoretical simulations demonstrated that the light extraction of both TE and transverse magnetic (TM) modes were improved by reflection, and the sideward light can be deflected upward by scattering by the etched nanovoids. Especially, the TM mode light was more extracted by NP-DBRs. Our work highlighted the possible applications enabled by the DUV NP-DBRs in light reflection and structural reconstructions of AlGaN-based UV emitters.

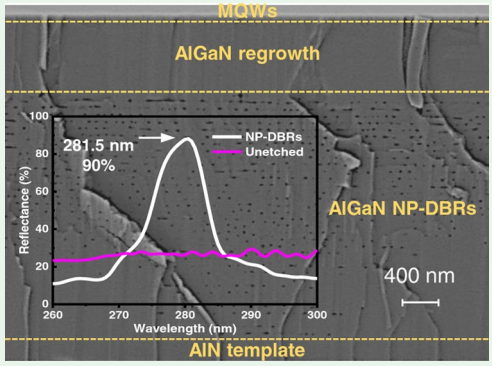

KEYWORDS: *deep ultraviolet, distributed Bragg reflectors, electrochemical etching, nanoporous AlGaN, TE and TM modes, light extraction*

■ INTRODUCTION

Ultraviolet (UV) distributed Bragg reflectors (DBRs) with high reflectance are essential building blocks to fabricate the vertical-cavity surface-emitting lasers (VCSELs),[1,2] resonant-cavity light-emitting diodes (RCLEDs),[3] resonant-cavity photodiodes (RCPD),[4] and the exciton-polariton lasers.[5] For vertical UV LEDs with transparent p-AlGaN, UV DBRs can be used to reflect the downward-traveling light upward, thus enhancing light extraction.[6] Among the III−V nitrides, UV DBRs are usually formed by alternately stacking AlGaN layers with different Al contents, which are hindered by large lattice mismatch, strain accumulation, poor quality, and low refractive index contrast.[7,8] So far, $Al_xGa_{1-x}N/Al_yGa_{1-y}N$ ($0.45 \leq x < y \leq 1$) DUV DBRs have been rarely reported, as well as the VCSELs and other microcavity emitters.[9] The only reported DUV VCSEL is implemented by transferring AlGaN multiple quantum wells (MQWs) into a dielectric cavity due to the lack of the as-grown AlGaN DBRs,[10] which degrades the quality of MQWs in the film liftoff process. Therefore, the preparation of high-reflectance DUV DBRs without epitaxy constraints and complex techniques is in need for UV light reflection and microcavity applications.

Introducing air voids in bulk materials to act as the low-refractive-index layers of DBRs could be an alternative approach.[11,12] For example, the n^+-GaN/GaN NP-DBRs are widely prepared by the doping-selective electrochemical (EC) etching process.[13,14] The n^+-GaN layers are heavily doped to $\sim 10^{20}$ cm^{-3}, and the GaN layers are lesser or not doped.[15] Thus, the former can be selectively electrochemically etched into porous structures with air voids, while the latter still remains unetched. In this way, the epitaxy constraints can be avoided by the doping periodic change rather than the composition change, and a low refractive index is achieved by the porosification of the heavily doped layers. By adjusting the layer thickness, GaN NP-DBRs with a photonic band gap ranging from visible to near UV spectra have been demonstrated, and they were widely integrated into VCSELs,[16,17] LEDs,[18,19] and RCPD,[20,21] thanks to their high

Received: June 20, 2022
Accepted: June 27, 2022
Published: July 7, 2022

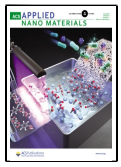

https://doi.org/10.1021/acsanm.2c02689
ACS Appl. Nano Mater. 2022, 5, 10081−10089

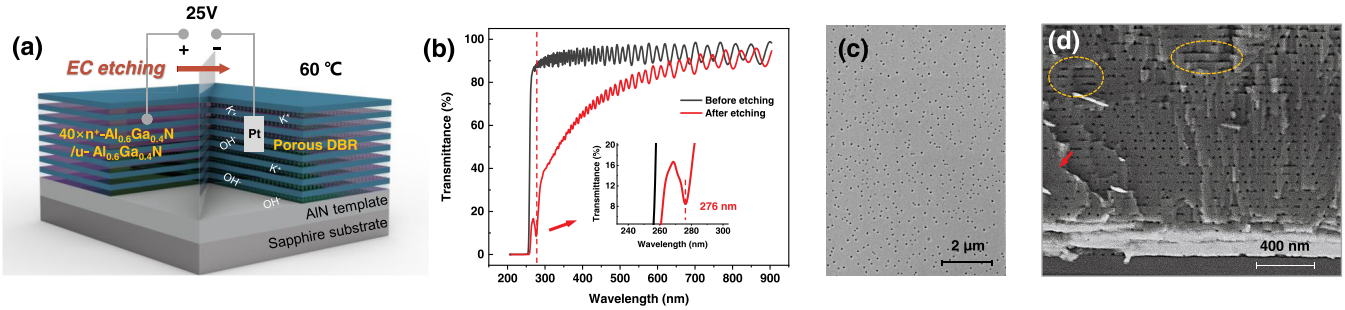

Figure 1. (a) Schematic diagram for the structure and fabrication of AlGaN-based NP-DBRs. (b) Transmittance spectra of the epitaxial DBRs before and after EC etching. (c) Top-view and (d) cross-sectional scanning electron microscopy (SEM) images of the electrochemically etched AlGaN NP-DBRs.

reflectance over 95%. It is the good etching selectivity and thus the large index contrast that pave the way for the high-performance GaN-based NP-DBRs. Furthermore, considering band-edge absorption, an AlGaN system with a larger band gap is required when the reflective spectra extend to the middle and deep UV regions.

However, the situation is not satisfactory in the AlGaN material, where the Si doping concentration (N_D) decreases with the increasing Al content due to the reduced dopant solubility, increased compensation, and the possible existence of DX levels.[22] Therefore, the *n*-AlGaN/AlGaN stacks with the Al content of over 45% have poor etching selectivity, that is, the etched *n*-AlGaN layers have low porosity, and the index contrast with unetched AlGaN layers is limited. As a result, the AlGaN NP-DBRs with stopband in the DUV regions are subjected to low reflectance. Few studies have reported reflectance close to 90%, but with Al content not exceeding 15%[19,23] and stopband staying at near UV.[24] Recently, Wu et al. have reported the lateral electrochemically etched n^+-$Al_{0.47}Ga_{0.53}N$/*n*-$Al_{0.47}Ga_{0.53}N$ DUV NP-DBRs with 93% reflectance at 276 nm.[25] The N_d of the n^+-$Al_{0.47}GaN$ and *n*-$Al_{0.47}GaN$ layers were 2×10^{19} and 5×10^{18} cm^{-3}, respectively. Although lateral EC etching is more favorable to achieve high porosity, separated mesas that are tens to hundreds of μm wide are disadvantageous for fabricating large-scale DBRs and related devices.

In this work, we demonstrated a wafer-scale *n*-$Al_{0.6}Ga_{0.4}N$/*u*-$Al_{0.6}Ga_{0.4}N$ DUV NP-DBRs by vertical EC etching. The stopbands were centered around 280 nm with reflectance close to 90%. Subsequently, a thick AlGaN film and MQWs structures were grown on the NP-DBRs to estimate the light reflection, where the photoluminescence (PL) intensity was more than twice that of the counterparts without NP-DBRs. To further analyze the light enhancement, the strain modulation and optical anisotropy of the emission from MQWs, as well as the light extraction by NP-DBRs were studied in detail.

■ EXPERIMENTAL DETAILS

The epitaxial structures were grown on a 2 in *c*-plane sapphire substrate (double-polished) by a metal−organic chemical vapor deposition (MOCDV) system. Trimethylaluminium, trimethylgallium, and ammonia were used as the precursors of Al, Ga, and N, respectively. Hydrogen served as the carrier gas. As shown in Figure 1a, a 1.5 μm AlN template was first deposited at 1250 °C as the buffer layer. Next, the stack DBRs comprising 40 periods of *n*-$Al_{0.6}Ga_{0.4}N$/*u*-$Al_{0.6}$Ga0.4N layers were grown at 920 °C. The thickness of the *n*-$Al_{0.6}Ga_{0.4}N$ and *u*-$Al_{0.6}Ga_{0.4}N$ layers were 32 and 27 nm, respectively. The Si doping concentration (N_D) in the *n*-$Al_{0.6}Ga_{0.4}N$ layers was 5×10^{18} cm^{-3}. The EC etching process was performed in a 5 wt % KOH solution at 25 V for 5 min, with indium contact DBRs as the anode and a platinum plate as the cathode. It is worth mentioning that the electrolyte was heated to 60 °C in this work to accelerate the N-polar chemical etching of the electrochemically etched nanovoids in *n*-$Al_{0.6}Ga_{0.4}N$ layers. As a result, DUV NP-DBRs with high porosity and good periodicity were obtained by a combination of EC etching and chemical etching processes, which are different from the previous NP-DBRs mainly prepared by EC etching. After etching, the wafer was immersed in a diluted HCl solution to remove the metal contact, then rinsed with deionized water, and dried using N_2. Next, the wafer was loaded back into the MOCVD chamber for subsequent growth. The regrown *u*-$Al_{0.6}Ga_{0.4}N$ film was deposited at 920 °C, and four-period $Al_{0.45}Ga_{0.55}N$/$Al_{0.65}Ga_{0.35}N$ MQWs were grown at 865 °C. The widths of the well and barrier were 2 and 10 nm, respectively.

The reflectance spectra of the NP-DBRs were measured using a UV−vis near-infrared spectrophotometer (Lambda 35). A scanning electron microscope (SEM, Nova Nano-SEM 450) and an atomic force microscope (AFM, SPM9700) were used to investigate the morphology of the NP-DBRs. The reciprocal space maps (RSMs) of the asymmetric (105) reflection were measured by high-resolution X-ray diffraction (HRXRD, PANalytical PW3040-60 MRD). The angle-resolved PL measurements were performed using a 193 nm ArF excimer laser (5 ns pulses at 50 Hz) as an excitation source. The sample was fixed on an angle-resolution bracket, and the optical fiber was placed near the sample at a distance of 10 cm. A Glan−Taylor prism was placed between the sample and the optical fiber to resolve the difference in polarized light. The PL signal was collected into a charge-coupled device (CCD) camera through a Horiba iHR550 spectrometer.

■ RESULTS AND DISCUSSION

Figure 1b shows the transmittance spectra of the wafer before and after EC etching. Before etching, the uniform interference fringes with a steep absorption edge at 255 nm indicate the high quality and high Al content of the DBRs. After etching, the transmittance decreased at a shorter wavelength due to strong scattering by the introduced air voids in *n*-$Al_{0.6}Ga_{0.4}N$ layers. At the same time, there is a minimal transmittance value around 276 nm, which is caused by the reflection of the incident light, a preliminary hint at the formation of DBRs. Figure 1c shows the top-view SEM image of the etched region, where densely distributed nanopores are observed on the top *u*-$Al_{0.6}Ga_{0.4}N$ layer. These surface nanopores are the initial etch pits that serve as openings for the electrolyte to penetrate downward. Figure 1d illustrates the cross-sectional SEM image of the etched NP-DBRs. It can be seen that the n^+-$Al_{0.6}Ga_{0.4}N$ layers are selectively etched into porous morphology with transversely distributed air voids, while the *u*-$Al_{0.6}Ga_{0.4}N$ layers are almost intact during the etching process. Only a few etch voids are connected, as marked by the yellow dotted circles,

https://doi.org/10.1021/acsanm.2c02689
ACS Appl. Nano Mater. 2022, 5, 10081−10089

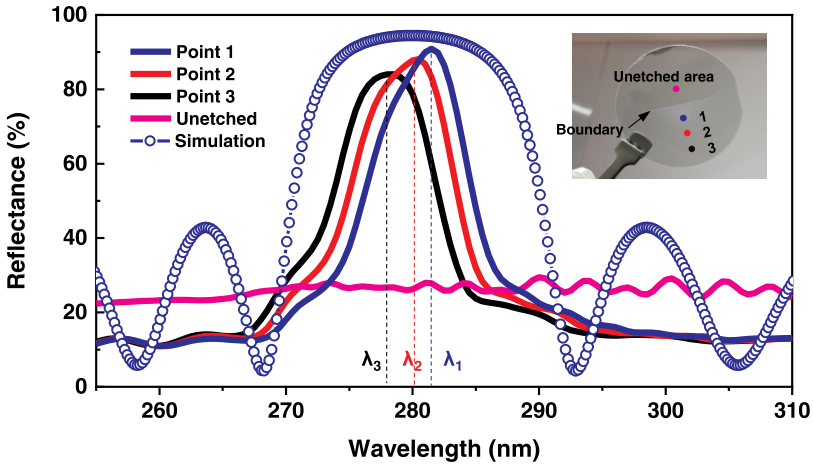

Figure 2. Reflectance of the AlGaN NP-DBRs in etched and unetched regions. The inset shows a photograph of a half-etched DBR wafer.

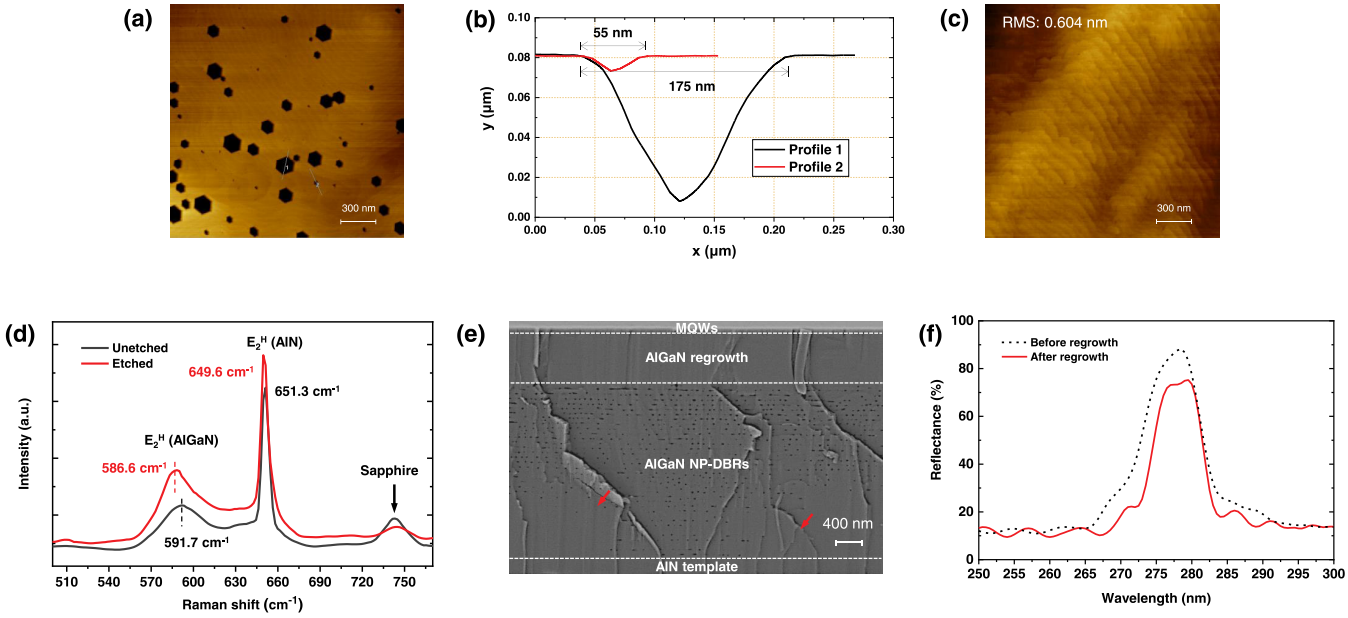

Figure 3. (a) AFM image of the DBRs in the etched region. (b) Horizontal and vertical profiles of the surface pits. (c) AFM image of the MQWs grown on etched NP-DBRs. (d) Raman spectra of the DBRs in etched and unetched regions. (e) Cross-sectional SEM image of the regrown structures on NP-DBRs. (f) Reflectance spectra of point 2 in the Wi-D region before and after regrowth.

and most voids are still discrete. The nearly triangular etch voids caused by the anisotropic etching due to the exposure of low-energy planes $\{10\bar{1}1\}$ by the EC etched nanovoids,[19] demonstrating the N-polar chemical etching along the opposite direction of the EC etching. The diameter of the etch voids is much smaller than the reflection wavelength, thus the porous layer can be considered as a homogeneous material with a constant refractive index. According to the volume average theory (VAT), the effective refractive index (n_{eff}) of the porous n-$Al_{0.6}Ga_{0.4}N$ can be estimated by[26] $n_{\mathrm{eff}} = [(1 - \varphi)n_{\mathrm{AlGaN}}^2 + \varphi n_{\mathrm{air}}^2]^{1/2}$, where φ is the porosity and n_{AlGaN} of the bulk $Al_{0.6}Ga_{0.4}N$ is 2.6 according to Brunner et al.[27] The porosity of the etched n-$Al_{0.6}Ga_{0.4}N$ layers is estimated to be 35% from the SEM image. Then, the n_{eff} is calculated to be 2.18, and the index contrast with unetched u-$Al_{0.6}Ga_{0.4}N$ is 0.42, even larger than that contrast with AlN.

The inset of Figure 2 shows a photograph of a wafer-scale DBRs which is half-etched for comparisons on either side of the boundary. In the etched region, three points (labeled points 1−3, respectively) were selected from the center to the edge to obtain the reflectance spectra. It can be seen in Figure 2 that the stopbands were centered around 280 nm with peak reflectance close to 90%, which undoubtedly demonstrates the formation of DBRs. However, the stopband width and peak reflectance are still lower compared to the GaN-based NP-DBRs, as the etch voids in n-$Al_{0.6}Ga_{0.4}N$ layers are discrete unlike the almost continuous ones in n^+-GaN,[28] mainly due to the limited N_D. In spite of this, there is still room for improving the porosity of AlGaN-based NP-DBRs by further optimizing the etching temperature and anodization voltage. The mismatch between simulation and experiment is due to the finite disorder in the spatial distribution of the etch voids in NP-DBRs. From points 1−3, the peak reflectance decreases from 90 to 84% and the stopband center (λ) blue shifts from 281.5 to 278 nm. These slight fluctuations may be caused by the voltage drop and doping inhomogeneity across the sample, which can be improved in future works. In the unetched region, the symmetric point of point 2 was selected as a

https://doi.org/10.1021/acsanm.2c02689
ACS Appl. Nano Mater. 2022, 5, 10081−10089

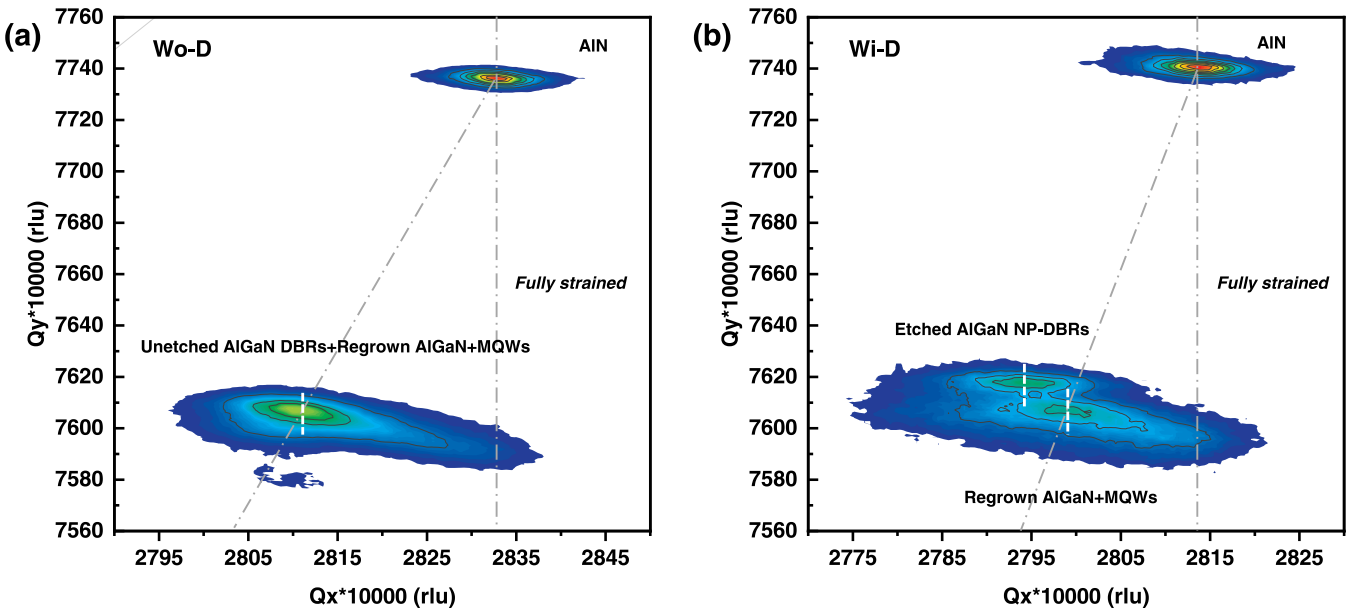

Figure 4. RSM of the regrown structures in regions (a) without and (b) with NP-DBRs.

comparison, and the reflectance is measured at about 25% with interference fringes due to the Fabry−Pérot effect at air/epilayer/sapphire interfaces.

To further probe the surface morphology of the etched region, a 2 μm × 2 μm AFM scan was performed, and the image is shown in Figure 3a. The etch pits are hexagonal in shape and vary in size. A line is drawn along the diagonal of the hexagon on the largest and smallest pits, and the horizontal and vertical profiles are extracted in Figure 3b. It can be seen that the pits are V-shaped and range in width from 55 to 175 nm. Such a large width of the pits is due to full contact with an electrolyte, and more importantly, the increase in etching temperature. In addition, the V-shaped pits own the smallest curvature radius at the bottom and thereby the strongest electric field. Therefore, Zener tunneling occurs and provides a large amount of hole charge (h^+) for anodization,[29] allowing vertical EC etching to rapidly proceed downward. No changes in the surface morphology are observed in regions without etch pits, manifesting that the surface was not fully damaged. Raman spectra measured in the etched and unetched regions are shown in Figure 3d. The typical E_2^H AlN peaks were measured at 649.6 and 651.3 cm^{-1} for the etched and unetched regions, respectively, which were both blue shifted versus the unstressed AlN (657.4 cm^{-1}). This Raman shift shows that the AlN buffers grown on the lattice-mismatched sapphire substrate are in the tensile status, and the one in the etched region is subjected to larger tensile stress. Compared to the unetched region (591.7 cm^{-1}), the E_2^H $Al_{0.6}Ga_{0.4}N$ peak of the etched region (586.6 cm^{-1}) shifts to a lower frequency, indicating the strain relaxation of NP-DBRs during the porosification process. Therefore, such NP-DBRs are not only able to provide the reflection effect but also show promise to act as a strain-relaxed template for the subsequent growth of MQWs, favoring high quality and strain modulation.[30]

To build the MQWs on the half-etched wafer, a 1 μm *u*-$Al_{0.6}Ga_{0.4}N$ film was first grown to fill the surface pits in the etched region. Then, four-period $Al_{0.45}Ga_{0.55}N/Al_{0.65}Ga_{0.35}N$ MQWs were capped on the thick AlGaN film, with the emission wavelength aligned with the stopband center of NP-DBRs. Figure 3e shows the cross-sectional SEM image of the regrown structures on the etched region. As the bottom NP-DBRs lost fracture toughness, the wafer could not be cleaved along a fixed plane, and the etch voids of a large area are obscured by other cross sections as indicated by the red arrows. It is worth noting that the shape transformation of etch voids can be induced during the regrowth by the annealing effects. As shown in Figure 3e, the size of the etch voids is shrunken as the triangular voids transformed into a circular shape due to the mass transport process.[31] As a result, the reflectance spectrum of point 2 in the Wi-D region exhibits a lower peak reflectance and a narrower stopband after the regrowth as shown in Figure 3f. Figure 3c shows the surface morphology of the MQWs grown on NP-DBRs, which was characterized by a 2 μm × 2 μm AFM scan, the root mean square roughness (RMS) of ∼0.604 nm, and the absence of pits.

To explore the strain modulation of MQWs grown on NP-DBRs, the XRD asymmetric (105) RSM were measured in regions without (Wo-D) and with NP-DBRs (Wi-D), and the results are shown in Figure 4a,b, respectively. In the (105) reflection, the lattice constants a and c of epilayers can be derived from the coordinate of the peak position (Q_x, Q_y) as follows[32]

$$a = \lambda/\sqrt{3}Q_x, \quad c = 5\lambda/2Q_y \tag{1}$$

where a_{AlN} in both regions are larger than a^0_{AlN} of unstressed AlN, indicating the tensile status of AlN buffers. In addition, a_{AlN} in the etched region is larger than that in the unetched region due to the strain-induced lattice expansion of the NP-DBRs, and more tensile stress is thus created under the AlN layer, which agrees well with the Raman results. The in-plane strain relaxation R% of the AlGaN layers with respect to the AlN buffer can be estimated by[33]

$$R\% = (a_{AlGaN} - a_{AlN})/(a^0_{AlGaN} - a^0_{AlN}) \tag{2}$$

where a^0_{AlGaN} of unstressed AlGaN can be determined according to Vegard's law.[34] As depicted in Figure 4a, the *u*-$Al_{0.6}Ga_{0.4}N$ film and MQWs are coherently grown on the unetched DBRs, since they share the same Q_x, and the strain

https://doi.org/10.1021/acsanm.2c02689
ACS Appl. Nano Mater. 2022, 5, 10081−10089

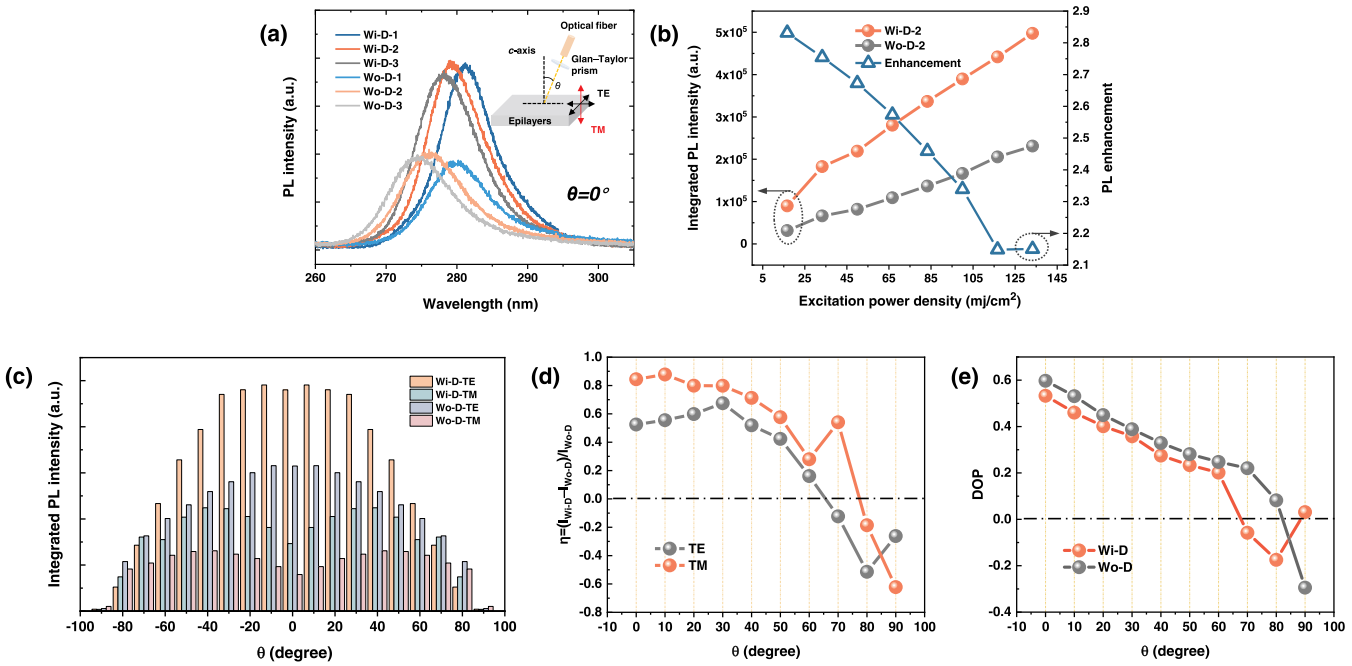

Figure 5. (a) PL spectra from the Wi-D and Wo-D regions. (b) Integrated PL intensity and PL enhancement as a function of excitation power density. (c) Full spatial TE/TM mode light intensity distributions in the Wi-D and Wo-D regions. (d) Increment η and (e) DOP as a function of θ.

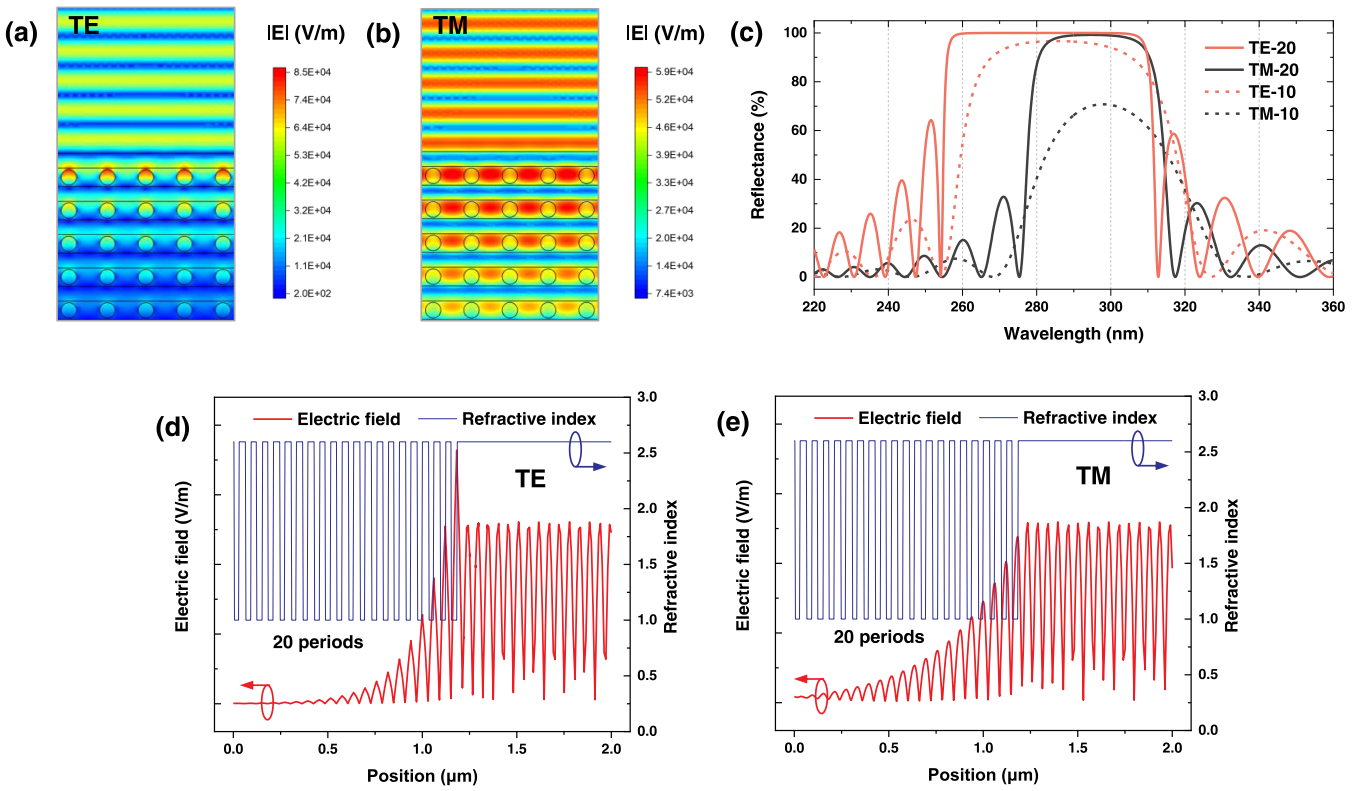

Figure 6. Electric field distribution and vertical electric field profiles simulated by Comsol multiphysics: (a and d) for the TE mode and (b and e) for the TM mode. (c) Simulated reflectance of 10- and 20-period NP-DBRs for TE and TM modes.

relaxation R% is calculated to be 79.2% for the MQWs. In Figure 4b, there is a distinct break in the strain between the etched NP-DBRs and regrown structures, as evidenced by the double AlGaN peaks. The Q_x of the u-$Al_{0.6}Ga_{0.4}N$ film and MQWs is red shifted versus the etched NP-DBRs, indicating the compressive status of the regrown structures on NP-DBRs, and R% is calculated to be 54.3% for the MQWs. These RSM results manifest that the MQWs grown on the NP-DBRs are of the lower strain relaxation, thus more compressive strain is reserved, which, is beneficial to the transverse electric (TE, $E \perp c$) polarized emission and surface light extraction of AlGaN-based UV emitters.[35]

https://doi.org/10.1021/acsanm.2c02689
ACS Appl. Nano Mater. 2022, 5, 10081−10089

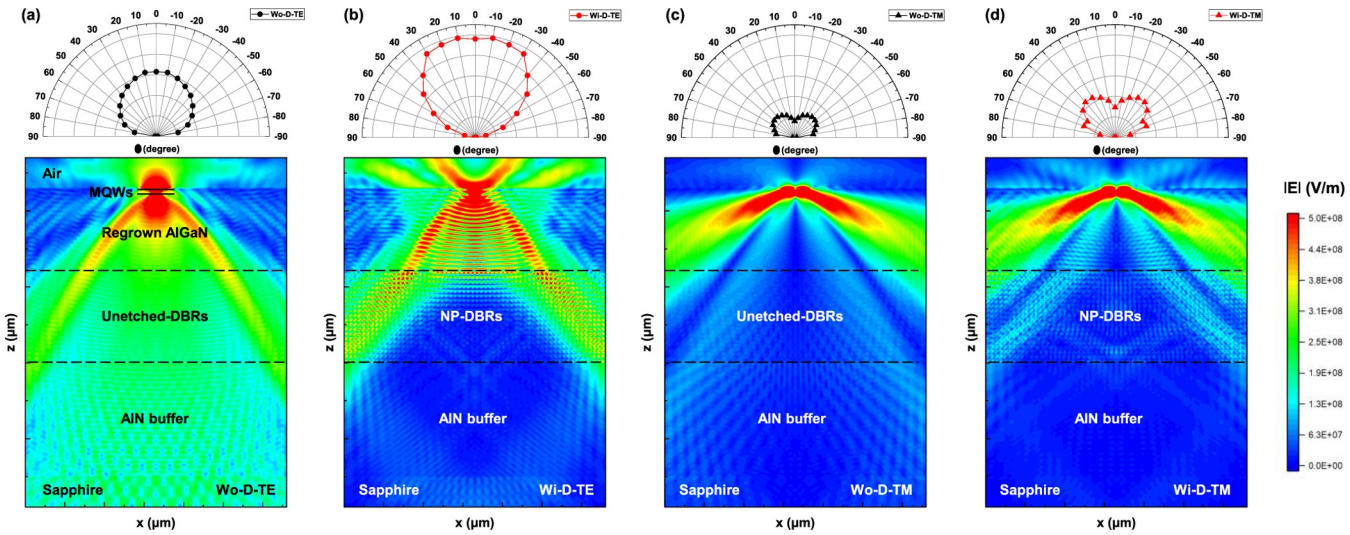

Figure 7. Cross-sectional distributions of electric field amplitude |*E*| of TE and TM modes simulated by Comsol Multiphysics: (a and c) for the Wo-D region and (b and d) for the Wi-D region. The experimental results are shown in upper polar diagrams, respectively.

To experimentally compare the light extraction in Wi-D and Wo-D regions, Figure 5a shows the PL spectra measured at $\theta = 0°$ under an excitation power density of 133 mj/cm^2, where θ is the angle between the optical fiber and the *c*-axis of epilayers as illustrated in the inset. The data were recorded from the labeled points (points 1−3) in the Wi-D region and the symmetry points in the Wo-D region. As shown in Figure 5a, the PL intensity in the Wi-D region is more than twice that in the Wo-D region, as the light traveling downward is reflected by the bottom NP-DBRs and exits from the top side. The red-shift of the peak wavelength in the Wi-D region accounts for the compressive strained MQWs revealed by the RSM results. Figure 5b shows the integrated PL intensity ($\theta = 0°$) that varies with the excitation power density in the Wi-D and Wo-D regions. The PL enhancement, described as $I_{\text{Wi-D}}/I_{\text{WO-D}}$ (I represents the integrated PL intensity), reaches as high as 2.83 at the lowest excitation power, which, is far beyond the light enhancement caused by the reflection of NP-DBRs. However, the PL enhancement shows a decreasing trend with the increase in the excitation power density due to the increased optical-transition matrix elements for transverse magnetic (TM, $E \| c$) mode at high carrier density,[36] where the TM photons mainly travel laterally. To probe the strain modulation of MQWs from the perspective of anisotropic optical polarization, the far-field distributions of full spatial TE/TM mode light in the Wi-D and Wo-D regions are measured at 133 mj/cm^2. It is demonstrated in Figure 5c that the NP-DBRs can strongly enhance the light extraction of both TE and TM modes thanks to the reflection effect. The increment η is defined as $\eta = (I_{\text{Wi-D}} - I_{\text{WO-D}})/I_{\text{WO-D}}$, and the results are shown in Figure 5d. It can be seen that the increments are almost negative at $\theta \geq 70°$ but positive at $\theta \leq 60°$, which features the small reflection angle of the $\lambda/4$ NP-DBRs. As a result, the sideward light cannot be reflected but is scattered by the introduced air voids, leading to the negative increments at $\theta \geq 70°$. Nevertheless, it is worth noting that the increments of TM mode are larger than those of the TE mode when $\theta \leq 80°$, which is intuitively against the TE dominant emission. About this point, Elafandy et al. have reported that the laterally etched GaN NP-DBRs (25 periods) with parallelly aligned cylindrical nanopores exhibit an anisotropic enhancement of the polarized light because the n_{eff} and thus the reflectance are different for incident light with the electric field tangential (TE) and normal (TM) to the nanopores.[37]

To clarify whether the anisotropic enhancement acts in the vertically etched AlGaN NP-DBRs with discrete nanovoids, Comsol multiphysics was used for the modeling analysis. To simplify the simulation, the etched air voids in *n*-AlGaN layers were approximated as the distributed circular sections with certain radii and intervals, and the porosity was kept consistent with the SEM result. A plane wave with a wavelength of 280 nm was placed on the regrown *u*-AlGaN layer as the light source. Figure 6a,b shows the electric field distributions within the 20-period NP-DBRs for TE and TM modes, respectively. The standing waves formed above the NP-DBRs for both modes demonstrate the good reflection effect. The vertical electric field profiles across the air voids are plotted in Figure 6d,e. Compared to the TE mode, the TM mode presents a slower decay and thus a longer penetration depth within NP-DBRs. Beyond that, the field leakage is more severe at intervals between adjacent voids for the TM mode, which, again implies the lower reflectance for this mode. The reflectance spectra for TE and TM modes, simulated at the setting of 10- and 20-period DBRs, are shown in Figure 6c. The reflectance spectra exhibit an obvious anisotropic enhancement, where the TM mode is red shifted with a narrower stopband and lower reflectance compared to the TE mode. However, the reflectance difference between the two modes decreases with the increase in the DBR periods and has reduced to 0.8% at 20 periods as shown in Figure 6c. As a result, when the period is sufficiently increased, such as the 40 periods in this work, the peak reflectance is believed to show no difference between the TE and TM modes. This inference means that the anisotropic enhancement in terms of reflection effect is not responsible for the increment difference of different polarized lights. Other extraction mechanisms of the TM mode are expected to be induced by the NP-DBRs,[38] where TM photons escape from the surface despite traveling mainly in the lateral direction. This may also account for the larger increment in the TM mode than that in the TE mode at $\theta = 70$ and 80°.

To acquire deep insight into the effect of NP-DBRs on light extraction, the cross-sectional electric field profiles of TE and

https://doi.org/10.1021/acsanm.2c02689
ACS Appl. Nano Mater. 2022, 5, 10081−10089

TM modes are simulated, and the results are shown in Figure 7. In these simulations, a dipole with different polarizations is placed at the center of MQWs to act as the light source. In the Wi-D region, the downward TE photons are almost fully reflected, as the electric field amplitude $|E|$ is weakly distributed in the AlN buffer and sapphire substrate, but strongly distributed above the NP-DBRs as shown in Figure 7b. The surface electric field of the TM mode is also significantly enhanced at $\theta \leq 60°$, but weakly distributed below the NP-DBRs, thanks to the high reflectance. However, the sideward TM mode that cannot be reflected is strengthened at $\theta = 70$ and 80° as well, and its traveling direction is deflected upward, as shown in Figure 7d. This light deflection effect can also be seen in the TE mode in the Wi-D region (Figure 7a), where TE photons weakly escape from the surface at $\theta \geq 70°$, along with an obvious change in the isotropous travel property in the Wo-D region. On the whole, the light travels laterally in the Wi-D region, especially the TM mode tends to be "pulled" upward, which is related to the scattering effect of the introduced air voids.[39] Such a deflected light can be more extracted from the surface, contributing to the extra light enhancement in addition to the reflection effect. These simulation results prove that the NP-DBRs can significantly improve the extraction of both TE and TM modes, and the TM photons can be more extracted from the surface, which matches well with the experimental results shown in the polar diagrams.

The degree of polarization (DOP) is calculated as DOP = $(I_{TE} - I_{TM})/(I_{TE} + I_{TM})$, and the results are shown in Figure 5e. In view of the reflection and the scattering effect, the DOP of MQWs can be relatively compared at $\theta = 90°$. The positive value (0.03) in the Wi-D region versus the negative value (−0.29) in the Wo-D region confirms the increased TE mode emission and the effective strain modulation of MQWs grown on NP-DBRs. However, corresponding to the more extraction of the TM mode by NP-DBRs, the DOP in the Wi-D region is inversely lower than that in the Wo-D region. Also, the negative DOP in the Wi-D region at $\theta = 70$ and 80° is caused by the reduced TE mode by scattering as well.

■ CONCLUSIONS

The wafer-scale AlGaN-based DUV NP-DBRs are successfully fabricated by vertical EC etching. The stopbands center near 280 nm with reflectance close to 90%. The MQWs grown on the strain-relaxed NP-DBRs exhibit increased compressive strain and thus enhanced TE mode emission. The PL intensity in the Wi-D region is more than twice that in the Wo-D region, and the light extraction of both TE and TM modes is improved thanks to the reflection effect by NP-DBRs. In addition, the TM mode can be more extracted from the surface due to the light deflection effect via scattering by the introduced air voids. Such highly reflective and easy-to-fabricate DUV NP-DBRs have promising applications in UV optoelectronic devices such as VCSELs and RCLEDs.

■ AUTHOR INFORMATION

Corresponding Authors

Feng Wu − *Wuhan National Laboratory for Optoelectronics, Huazhong University of Science and Technology, Wuhan 430074, China*; Email: wufeng123@hust.edu.cn

Xiaohang Li − *Advanced Semiconductor Laboratory, King Abdullah University of Science and Technology (KAUST), Thuwal 23955, Saudi Arabia*; orcid.org/0000-0002-4434-365X; Email: xiaohang.li@kaust.edu.sa

Changqing Chen − *Wuhan National Laboratory for Optoelectronics, Huazhong University of Science and Technology, Wuhan 430074, China*; Email: cqchen@hust.edu.cn

Authors

Maocheng Shan − *Wuhan National Laboratory for Optoelectronics, Huazhong University of Science and Technology, Wuhan 430074, China; Advanced Semiconductor Laboratory, King Abdullah University of Science and Technology (KAUST), Thuwal 23955, Saudi Arabia*

Chenyu Guo − *Ningbo Institute of Materials Technology and Engineering, Chinese Academy of Sciences, Ningbo 315201 Zhejiang, China; University of Science and Technology of China, Hefei 230026 Anhui, China*

Yongming Zhao − *Wuhan National Laboratory for Optoelectronics, Huazhong University of Science and Technology, Wuhan 430074, China*

Qiushuang Chen − *Ningbo Institute of Materials Technology and Engineering, Chinese Academy of Sciences, Ningbo 315201 Zhejiang, China*

Liqiong Deng − *Ningbo Institute of Materials Technology and Engineering, Chinese Academy of Sciences, Ningbo 315201 Zhejiang, China*

Zhihua Zheng − *Wuhan National Laboratory for Optoelectronics, Huazhong University of Science and Technology, Wuhan 430074, China*

Shizhou Tan − *Wuhan National Laboratory for Optoelectronics, Huazhong University of Science and Technology, Wuhan 430074, China*

Wei Guo − *Ningbo Institute of Materials Technology and Engineering, Chinese Academy of Sciences, Ningbo 315201 Zhejiang, China*; orcid.org/0000-0002-6233-0529

Jiangnan Dai − *Wuhan National Laboratory for Optoelectronics, Huazhong University of Science and Technology, Wuhan 430074, China*; orcid.org/0000-0001-9805-8726

Complete contact information is available at: https://pubs.acs.org/10.1021/acsanm.2c02689

Notes

The authors declare no competing financial interest.

■ ACKNOWLEDGMENTS

This work is supported by the National Key Research and Development Program of China (Grant No. 2019YFA0708203), the Key Research and Development Program of Hubei Province (Grant No. 2021BAA071), the National Natural Science Foundation of China (Grant Nos. 62174061, 62174063, 61904184, and 61974174), the Fundamental Research Funds for the Central Universities (Grant No. 2020kfyXJJS124), and the Director Fund of WNLO.

■ REFERENCES

(1) Hjort, F.; Enslin, J.; Cobet, M.; Bergmann, M. A.; Gustavsson, J.; Kolbe, T.; Knauer, A.; Nippert, F.; Häusler, I.; Wagner, M. R.; Wernicke, T.; Kneissl, M.; Haglund, Å. A 310 nm Optically Pumped AlGaN Vertical-Cavity Surface-Emitting Laser. *ACS Photonics* **2021**, *8*, 135−141.

(2) Gębski, M.; Lott, J. A.; Czyszanowski, T. Electrically Injected VCSEL with a Composite DBR and MHCG Reflector. *Opt. Express* **2019**, *27*, 7139.
(3) Mastro, M. A.; Caldwell, J. D.; Holm, R. T.; Henry, R. L.; Eddy, C. R. Design of Gallium Nitride Resonant Cavity Light-Emitting Diodes on Si Substrates. *Adv. Mater.* **2008**, *20*, 115−118.
(4) Li, J.; Yang, C.; Liu, L.; Cao, H.; Lin, S.; Xi, X.; Li, X.; Ma, Z.; Wang, K.; Patanè, A.; Zhao, L. High Responsivity and Wavelength Selectivity of GaN-Based Resonant Cavity Photodiodes. *Adv. Opt. Mater.* **2020**, *8*, No. 1901276.
(5) Tao, R.; Kamide, K.; Arita, M.; Kako, S.; Arakawa, Y. Room-Temperature Observation of Trapped Exciton-Polariton Emission in GaN/AlGaN Microcavities with Air-Gap/III-Nitride Distributed Bragg Reflectors. *ACS Photonics* **2016**, *3*, 1182−1187.
(6) Cao, D.; Yang, X.; Shen, L.; Zhao, C.; Luan, C.; Ma, J.; Xiao, H. Fabrication and Properties of High Quality InGaN-Based LEDs with Highly Reflective Nanoporous GaN Mirrors. *Photonics Res.* **2018**, *6*, 1144.
(7) Franke, A.; Hoffmann, M. P.; Kirste, R.; Bobea, M.; Tweedie, J.; Kaess, F.; Gerhold, M.; Collazo, R.; Sitar, Z. High Reflectivity III-Nitride UV-C Distributed Bragg Reflectors for Vertical Cavity Emitting Lasers. *J. Appl. Phys.* **2016**, *120*, No. 135703.
(8) Liu, B.; Zhang, R.; Zheng, J. G.; Ji, X. L.; Fu, D. Y.; Xie, Z. L.; Chen, D. J.; Chen, P.; Jiang, R. L.; Zheng, Y. D. Composition Pulling Effect and Strain Relief Mechanism in AlGaN/AlN Distributed Bragg Reflectors. *Appl. Phys. Lett.* **2011**, *98*, No. 261916.
(9) Detchprohm, T.; Liu, Y.-S.; Mehta, K.; Wang, S.; Xie, H.; Kao, T.-T.; Shen, S.-C.; Yoder, P. D.; Ponce, F. A.; Dupuis, R. D. Sub 250 nm Deep-UV AlGaN/AlN Distributed Bragg Reflectors. *Appl. Phys. Lett.* **2017**, *110*, No. 011105.
(10) Zheng, Z.; Mei, Y.; Long, H.; Hoo, J.; Guo, S.; Li, Q.; Ying, L.; Zheng, Z.; Zhang, B. AlGaN-Based Deep Ultraviolet Vertical-Cavity Surface-Emitting Laser. *IEEE Electron Device Lett.* **2021**, *42*, 375−378.
(11) Chen, D.; Han, J. High Reflectance Membrane-Based Distributed Bragg Reflectors for GaN Photonics. *Appl. Phys. Lett.* **2012**, *101*, No. 221104.
(12) Zhang, C.; Park, S. H.; Chen, D.; Lin, D. W.; Xiong, W.; Kuo, H. C.; Lin, C. F.; Cao, H.; Han, J. Mesoporous GaN for Photonic Engineering-Highly Reflective GaN Mirrors as an Example. *ACS Photonics* **2015**, *2*, 980−986.
(13) Lee, S. M.; Kang, J. H.; Lee, J. K.; Ryu, S. W. Fabrication of High Reflectivity Nanoporous Distributed Bragg Reflectors by Controlled Electrochemical Etching of GaN. *Electron. Mater. Lett.* **2016**, *12*, 673−678.
(14) Zhu, T.; Liu, Y.; Ding, T.; Fu, W. Y.; Jarman, J.; Ren, C. X.; Kumar, R. V.; Oliver, R. A. Wafer-Scale Fabrication of Non-Polar Mesoporous GaN Distributed Bragg Reflectors via Electrochemical Porosification. *Sci. Rep.* **2017**, *7*, No. 45344.
(15) Yuan, G.; Zhang, C.; Xiong, K.; Han, J. InGaN/GaN Microdisks Enabled by Nanoporous GaN Cladding. *Opt. Lett.* **2018**, *43*, 5567.
(16) Lee, S.-M.; Gong, S.-H.; Kang, J.-H.; Ebaid, M.; Ryu, S.-W.; Cho, Y.-H. Optically Pumped GaN Vertical Cavity Surface Emitting Laser with High Index-Contrast Nanoporous Distributed Bragg Reflector. *Opt. Express* **2015**, *23*, 11023.
(17) Mishkat-Ul-Masabih, S. M.; Aragon, A. A.; Monavarian, M.; Luk, T. S.; Feezell, D. F. Electrically Injected Nonpolar GaN-Based VCSELs with Lattice-Matched Nanoporous Distributed Bragg Reflector Mirrors. *Appl. Phys. Express* **2019**, *12*, No. 036504.
(18) Fan, F.-H.; Syu, Z.-Y.; Wu, C.-J.; Yang, Z.-J.; Huang, B.-S.; Wang, G.-J.; Lin, Y.-S.; Chen, H.; Hauer Kao, C.; Lin, C.-F. Ultraviolet GaN Light-Emitting Diodes with Porous-AlGaN Reflectors. *Sci Rep.* **2017**, *7*, No. 4968.
(19) Lu, X.; Li, J.; Su, K.; Ge, C.; Li, Z.; Zhan, T.; Wang, G.; Li, J. Performance-Enhanced 365 nm UV LEDs with Electrochemically Etched Nanoporous AlGaN Distributed Bragg Reflectors. *Nanomaterials* **2019**, *9*, 862.
(20) Wu, C.-J.; Wang, G.-J.; Kao, C. H.; Yang, Z.-J.; Chen, H.; Lin, Y.-S.; Lin, C.-F.; Han, J. Photon-Recycling in Ultraviolet GaN-Based Photodiodes with Porous AlGaN Distributed Bragg Reflectors. *ACS Appl. Nano Mater.* **2019**, *2*, 5044−5048.
(21) Li, J.; Yang, C.; Liu, L.; Cao, H.; Lin, S.; Xi, X.; Li, X.; Ma, Z.; Wang, K.; Patanè, A.; Zhao, L. High Responsivity and Wavelength Selectivity of GaN-Based Resonant Cavity Photodiodes. *Adv. Opt. Mater.* **2020**, *8*, No. 1901276.
(22) Nam, K. B.; Li, J.; Nakarmi, M. L.; Lin, J. Y.; Jiang, H. X. Achieving Highly Conductive AlGaN Alloys with High Al Contents. *Appl. Phys. Lett.* **2002**, *81*, 1038−1040.
(23) Wang, G.-J.; Hong, B.-S.; Chen, Y.-Y.; Yang, Z.-J.; Tsai, T.-L.; Lin, Y.-S.; Lin, C.-F. GaN/AlGaN Ultraviolet Light-Emitting Diode with an Embedded Porous-AlGaN Distributed Bragg Reflector. *Appl. Phys. Express* **2017**, *10*, No. 122102.
(24) Griffin, P.; Zhu, T.; Oliver, R. Porous AlGaN-Based Ultraviolet Distributed Bragg Reflectors. *Materials* **2018**, *11*, 1487.
(25) Wu, C.-J.; Kuo, C.-Y.; Wang, C.-J.; Chang, W.-E.; Tsai, C.-L.; Lin, C.-F.; Han, J. Deep-UV Porous AlGaN Distributed Bragg Reflectors for Deep Ultraviolet Light-Emitting Diodes and Laser Diodes. *ACS Appl. Nano Mater.* **2020**, *3*, 399−402.
(26) Zhang, C.; Park, S. H.; Chen, D.; Lin, D.-W.; Xiong, W.; Kuo, H.-C.; Lin, C.-F.; Cao, H.; Han, J. Mesoporous GaN for Photonic Engineering—Highly Reflective GaN Mirrors as an Example. *ACS Photonics* **2015**, *2*, 980−986.
(27) Brunner, D.; Angerer, H.; Bustarret, E.; Freudenberg, F.; Höpler, R.; Dimitrov, R.; Ambacher, O.; Stutzmann, M. Optical Constants of Epitaxial AlGaN Films and Their Temperature Dependence. *J. Appl. Phys.* **1997**, *82*, 5090−5096.
(28) Cao, D.; Yang, X.; Shen, L.; Zhao, C.; Luan, C.; Ma, J.; Xiao, H. Fabrication and Properties of High Quality InGaN-Based LEDs with Highly Reflective Nanoporous GaN Mirrors. *Photon. Res.* **2018**, *6*, 1144.
(29) Tseng, W. J.; van Dorp, D. H.; Lieten, R. R.; Vereecken, P. M.; Borghs, G. Anodic Etching of N-GaN Epilayer into Porous GaN and Its Photoelectrochemical Properties. *J. Phys. Chem. C* **2014**, *118*, 29492−29498.
(30) Kawase, Y.; Ikeda, S.; Sakuragi, Y.; Yasue, S.; Iwayama, S.; Iwaya, M.; Takeuchi, T.; Kamiyama, S.; Akasaki, I.; Miyake, H. Ultraviolet-B Band Lasers Fabricated on Highly Relaxed Thick $Al_{0.55}Ga_{0.45}N$ Films Grown on Various Types of AlN Wafers. *Jpn. J. Appl. Phys.* **2019**, *58*, No. SC1052.
(31) Yerino, C. D.; Zhang, Y.; Leung, B.; Lee, M. L.; Hsu, T. C.; Wang, C. K.; Peng, W. C.; Han, J. Shape Transformation of Nanoporous GaN by Annealing: From Buried Cavities to Nanomembranes. *Appl. Phys. Lett.* **2011**, *98*, No. 251910.
(32) Dion, J.; Fareed, Q.; Zhang, B.; Khan, A. Structural Characterization of Highly Conducting AlGaN (x > 50%) for Deep-Ultraviolet Light-Emitting Diode. *J. Electron. Mater.* **2011**, *40*, 377−381.
(33) Moram, M. A.; Vickers, M. E. X-Ray Diffraction of III-Nitrides. *Rep. Prog. Phys.* **2009**, *72*, No. 036502.
(34) Angerer, H.; Brunner, D.; Freudenberg, F.; Ambacher, O.; Stutzmann, M.; Höpler, R.; Metzger, T.; Born, E.; Dollinger, G.; Bergmaier, A.; Karsch, S.; Körner, H. J. Determination of the Al Mole Fraction and the Band Gap Bowing of Epitaxial $Al_xGa_{1-x}N$ Films. *Appl. Phys. Lett.* **1997**, *71*, 1504−1506.
(35) Long, H.; Wang, S.; Dai, J.; Wu, F.; Zhang, J.; Chen, J.; Liang, R.; Feng, Z. C.; Chen, C. Internal Strain Induced Significant Enhancement of Deep Ultraviolet Light Extraction Efficiency for AlGaN Multiple Quantum Wells Grown by MOCVD. *Opt. Express* **2018**, *26*, 680.
(36) Park, S. H.; Shim, J. I. Carrier Density Dependence of Polarization Switching Characteristics of Light Emission in Deep-Ultraviolet AlGaN/AlN Quantum Well Structures. *Appl. Phys. Lett.* **2013**, *102*, No. 221109.
(37) Elafandy, R. T.; Kang, J.; Mi, C.; Kim, T. K.; Kwak, J. S.; Han, J. Study and Application of Birefringent Nanoporous GaN in the Polarization Control of Blue Vertical-Cavity Surface-Emitting Lasers. *ACS Photonics* **2021**, *8*, 1041−1047.

https://doi.org/10.1021/acsanm.2c02689
ACS Appl. Nano Mater. 2022, 5, 10081−10089

(38) Li, Y.; Wang, C.; Zhang, Y.; Hu, P.; Zhang, S.; Du, M.; Su, X.; Li, Q.; Yun, F. Analysis of TM/TE Mode Enhancement and Droop Reduction by a Nanoporous n-AlGaN Underlayer in a 290 nm UV-LED. *Photonics Res.* **2020**, *8*, 806.

(39) Zhang, L.; Guo, Y. N.; Yan, J. C.; Wu, Q. Q.; Wei, X. C.; Wang, J. X.; Li, J. M. Deep Ultraviolet Light-Emitting Diodes with Improved Performance via Nanoporous AlGaN Template. *Opt. Express* **2019**, *27*, 4917.

https://doi.org/10.1021/acsanm.2c02689
ACS Appl. Nano Mater. 2022, 5, 10081−10089